Magnetic coupling of spins in and between Co-Kagomé layers is studied from experiment and theory for $Sn_2Co_3S_{2-x}Se_2$. XRD, [119]Sn-Mößbauer, magnetic susceptibility, and DFT studies provide an inside into effects on the macroscopic and local scales.

Journal Name

ARTICLE

Tuneable anisotropy and magnetism in $Sn_2Co_3S_{2-x}Se_x$ – probed by ^{119}Sn Mößbauer Spectroscopy and DFT studies

Richard Weihrich,[a,b]* Wenjie Yan,[a] Jan Rothballer,[a] Philipp Peter,[a] Stefan Michael Rommel,[a] Sebastian Haumann,[a] Florian Winter,[c] Christian Schwickert,[c] Rainer Pöttgen[c]

Dedicated to Prof. Juri Grin on the occasion of his 60th birthday

The half metal (HFM) $Sn_2Co_3S_2$ shows a fascinating S = 1/2 magnetism. Anisotropic coupling of spins in and between Co Kagomé layers by Sn sites is now studied from substitution effects of S by Se by systematic and local experimental and first principle data. Trends in crystal structure changes (c/a ratio) as retrieved from XRD data on the solid solution $Sn_2Co_3S_{2-x}Se_x$ are complemented by DFT modelling on Sn_2Co_3SeS and hitherto unknown $Sn_2Co_3Se_2$. The relation of crystal structure effects to changes on Curie temperatures and magnetic hysteresis is shown from susceptibility measurements. Insight into the role of the Sn sites in magnetism and bonding is gained from ^{119}Sn Mössbauer spectroscopic measurements. Isomer shift, quadrupole splitting, and magnetic hyperfine fields are interpreted by DFT calculations on chemical bonding, electric field gradients (EFG), Fermi contact, and spin polarization.

Introduction

The combination of low dimensional crystal and tuneable electronic structures provides ways to fascinating magnetic and thermoelectric materials.[1] Here, chalcogenides $A_2M_3Ch_2$ classified as half antiperovskites (HAP)[2] $AM_{3/2}Ch$ with low dimensional $[M_3Ch_2]$ substructures turn into focus.[2-10] Besides superconducting parkerites $(Bi_2Ni_3S_2)$[3] the trigonal shandite $(Pb_2Ni_3S_2)$ type solid solution $In_xSn_{2-x}Co_yS_2$ attracts increasing attention.[4-10] Therein, thermoelectric $InSnCo_3S_2$ (46 valence electrons, VE) and half metal ferromagnetic $Sn_2Co_3S_2$ (47 VE) were predicted from DFT calculations.[4] They obey a |VE-46| electron counting rule[11] where additional electrons or holes are spin polarised with respect to semiconducting $InSnCo_3S_2$. A maximum in VE = 50 causes a breakdown of ferromagnetism for $Sn_2Ni_3S_2$ in line with the zero-valent state of Ni^0 (d^{10}).[12] For VE < 46 a way to magnetic design is shown for Fe containing shandites as proven by first experimental results.[13]

Magnetic anisotropy of $Sn_2Co_3S_2$ arises from the combination of an S = 1/2 half metal (HFM) ground state and its layered structure.[14-18] One must conclude that spins couple in and between Co Kagomé layers that are spaced to more than c/3 > 4

Å. According to oriented magnetic measurements on single crystals,[14,17] $Sn_2Co_3S_2$ can be magnetized only perpendicular to the Co layers. A local insight was provided by ^{119}Sn Mößbauer spectroscopy on two Sn sites in and between the layers. High transferred hyperfine fields up to 38 T were found with high quadrupole moments that remind to solid solutions and heterolayer devices.[18,19]

Substitution effects on the anisotropic structure and magnetic coupling within and between Co Kagomé layers were first seen for the solid solution $In_xSn_{2-x}Co_3S_2$.[4,6,10] Therein, electron counting effects and crystal structure distortions (c/a ratio) are superimposed. They are hardly distinguished and attributed to In/Sn ordering and local bonding effects for A = In, Sn sites.[20]

To address structure effects only, isoelectronic substitution of S by Se in $Sn_2Co_3S_2$ is subsequently studied. Effects of Se on magnetism are known e.g. for $CoS_{2-x}Se_x$ and $TlCo_2S_{2-x}Se_x$.[22-23] The recently reported solid solution $Sn_2Co_3S_xSe_{2-x}$[21] is well suited to gain closer insight into the magnetism of the Co shandites. Besides X-ray diffraction (XRD) and magnetic measurements ^{119}Sn-Mößbauer spectroscopy is subsequently combined with DFT calculations on crystal and electronic structures. Details in chemical bonding and charges are

discussed like the question on Sn(+II) states as claimed in non-magnetic $Sn_2Ni_3S_2$.[12] As only a few Se shandites like $Pb_2M_3Se_2$ (M = Ni, Rh, Pd)[2] are known the reported limit of x(Se) concerns phase stability of competing phases.[24]

Experimental

Sample preparation

The samples of the solid solution $Sn_2Co_3S_{2-x}Se_x$ were prepared by high temperature synthesis from the corresponding elements in sealed quartz ampoules.[4,20,24] They were heated to 550°C and cooled down slowly to room temperature after 5 days.

X-ray

X-ray powder diffraction on crushed and ground powders was performed with a Huber G670 diffractometer equipped with an imaging plate detector and Cu-$K_{\alpha 1}$-radiation (λ = 1.54060 Å, Ge-monochromator). Diffraction data were collected in a 2θ-range from 4.0° to 100°. Impurity phases can be assigned for x > 2. Refinement of the XRD powder data was done with the Rietveld method within the JANA program suite.[25]

Thermal analysis

Se substitution effects on Curie temperatures were investigated by DSC measurements (Mettler) for 120 K > T > 298 K.

Magnetic susceptibility measurements

Magnetic measurements were carried out using a Physical Property Measurement System (PPMS, Quantum Design) with a vibrating sample magnetometer. The measurements were performed in the temperature range of 3-300 K with flux densities up to 80 kOe. Suitable amounts of the polycrystalline samples were packed in polypropylene capsules and affixed to a brass sample holder rod for the measurement.

^{119}Sn Mössbauer spectroscopy

A Ca^{119}SnO$_3$ source was used for the ^{119}Sn Mössbauer spectroscopic investigation. The $Sn_2Co_3S_{2-x}Se_x$ samples were placed within thin-walled PMMA containers at a thickness of about 10 mg Sn/cm^2. A palladium foil of 0.05 mm thickness was used to reduce the tin K X-rays concurrently emitted by this source. The measurements were conducted in the usual transmission geometry at room temperature and 78 K.

Computational details

The first-principles electronic structure calculations were carried out within the framework of DFT with generalized gradient approximation (GGA) functionals as parameterized by Perdew-Burke-Enzerhof (PBE).[26] Full geometry optimizations, calculations of electric field gradients (EFG), and the electron localisation function (ELF) were executed with CRYSTAL14.[27] Band structure, spin polarized, and total energy calculations were performed with full potential local orbital FPLO package.[28-29] It is also used for orbital analysis as it optimises

basis functions automatically. A k-grid mesh of $12 \times 12 \times 12$ was applied to reach sufficient accuracy.

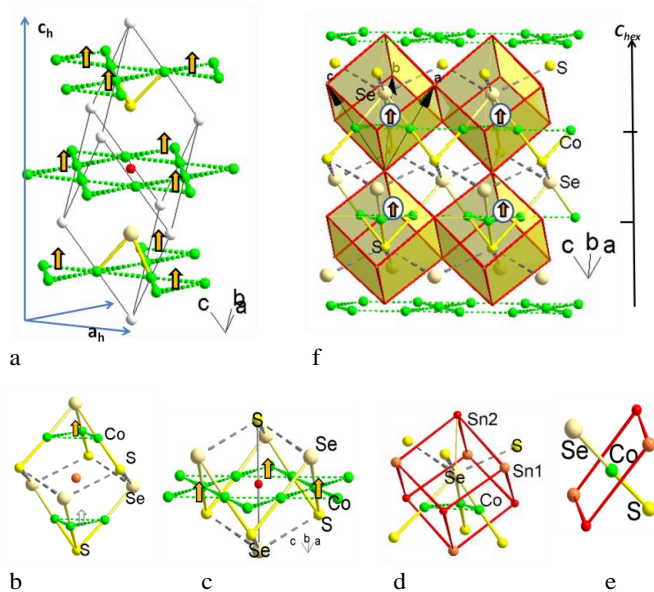## Results and discussion

Crystal structure effects for X = S, Se

Fig. 1. Crystal structure and magnetic coupling for Sn_2Co_3SeS with a) rhombohedral unit cell (a_{rh}, α_{rh}), hexagonal axes a_h, c_h; coordination spheres of b) Sn1, c) Sn2, d) Se, and e) Co; f) Sn substructure and magnetic coupling within and between Co Kagomé layers.

Fig. 1a introduces main questions on substitution effects in the solid solution $Sn_2Co_3S_{1-x}Se_x$. Therefore a rhombohedral cell of Sn_2Co_3SeS was obtained from $Sn_2Co_3S_2$[4] by replacement of half of the S atoms by Se. It is predicted as S = ½ half metal ferromagnetism (HFM) like $Sn_2Co_3S_2$ and hitherto unknown $Sn_2Co_3Se_2$ from DFT calculations (Tab. 1). The calculated net moment of 1 μ_B is due to additional electrons (visualized by arrows in Fig. 1) compared to semiconducting $InSnCo_3S_2$[4,6,8,9].

The chalcogen (*Ch*) atoms link Co triangles of Kagomé nets to [Co_3Ch_2] sheets. Selen will change the linear *Ch*-Co-*Ch* bonds therein that indicate Co(0). Effects on interlayer spacing (1/3 c_{hex}) and intralayer distances (d_{Co-Co}=½ a_{hex}) are probed from hexagonal cell parameters a_{hex}, c_{hex}.

What were role and effects of Co-Co, Sn-Co and Sn-*Ch* bonds in magnetic coupling, anisotropy, and valences? A key is found by ^{119}Sn Mößbauer spectroscopy on Sn sites between (Sn1) and in (Sn2) the Co layers. The inverted coordination by Co and S/Se atoms turns out decisive (Fig. 1b-c). It is signalled first from the Sn positions in distorted S/Se cages, second from a Laves[30] like [Sn_2Co_3] partial structure. Distances d_{Sn1-Co} = ½ a_{rh} and angles (Co-Sn1-Co) = α_{rh} are determined by the trigonal cell axes a_{rh} and α_{rh}. Sn1 (0/0/0) connects two Co triangles of neighbouring layers. Sn2 is found on (1/2,1/2,1/2) sites in Co

hexagons. Co-Co distances ($d_{Co-Co} = 2.7$ Å) in $Sn_2Co_3S_2$[2] are longer than in metal Co ($d_{Co-Co} = 2.50$ Å). Like in intermetallics CoSn (2.63 Å),[31] $CoSn_2$ (2.73 Å),[41] or Co_3Sn_2 (2.6-2.7 Å)[42] they are estimated weaker than Co-Sn. Sn-S distances of more than 3.0 Å in $Sn_2Co_3S_2$ are longer than for SnS (2.6-2.8 Å).

The hybride situation with metal-chalcogene and metal-metal bonds is accounted for by our concept of half antiperovskites (HAP).[2,4] It is based on the primitive Sn substructure (fig. 1d-f) centred by S and Se in $Sn_2Co_3S_{2-x}Se_x$. Co atoms on half of the Sn_4Ch_2 sites account for the stabilisation of Ch-Co-Ch by Co-Sn bonds (Fig. 1d). Vice versa, the Sn atoms in Ch = S, Se cages with 6 Co neighbours become comparable to Ca in perovskite ($CaTiO_3$), when 6 of the 12 O neighbours are removed.[2] Because of unoccupied Sn_4Ch_2 sites the shift z(Ch) along c_{hex} allows for flexibility and causes secondary Sn2-Ch bonds. The polyhedra are interlinked by faces within the layers and by Sn1 corners along c_{hex}. The scheme in Fig. 1f, should finally account for bonding and magnetism in $Sn_2Co_3S_{2-x}Se_x$.

a

b

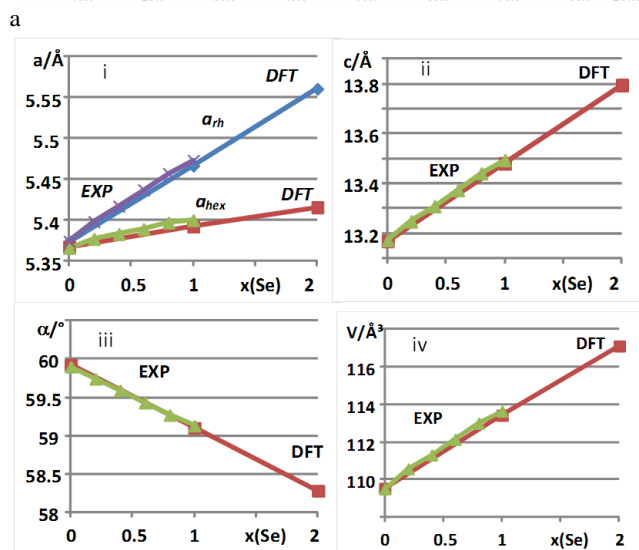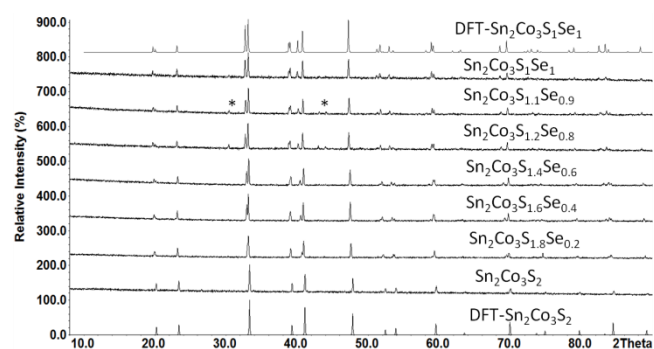**Fig. 2.** a) X-ray powder diffraction patterns for $Sn_2Co_3S_{2-x}Se_x$ samples (* mark impurities) and DFT models (x = 1, 0), b) cell parameters a_{hex} and a_{rh} (i), c_{hex}(ii), α_{rh} (iii), and V_{rh} (iv).

Experimentally, crystal structure effects for the substitution of S by Se in $Sn_2Co_3S_{2-x}Se_x$ are confirmed as well as limited soluability.[21] Diffraction patterns obtained for $0 \geq x \leq 1.0$

samples (Fig. 2a, Tab. 2) were refined for trigonal R centred shandite type cells. Minor impurities are attributed to SnSe, CoSn, and Co_3Sn_2. For x(Se) > 1 impurities become dominant (see ESI, S2-5). For $0 \geq x \leq 1.0$ samples splitting of reflections at 33° and 41° is related to trigonal distortions with increasing x(Se) in $Sn_2Co_3S_{2-x}Se_x$. As analysed in Fig. 2b all cell axis grow in line with Vegard´s law. Se induces higher anisotropy as indicated by diverging a_{rh} (5.37 to 5.47 Å) and a_{hex} (5.37 to 5.40 Å) axes (i, Tab. 2) and the increase of $c_{hex} = 13.17$ Å (x = 0) to 13.49 Å (x = 1) (ii). The decrease of trigonal angles (iii) from $\alpha_{rh} = 59.9°$ to 59.1° mirrors a change of $c_{hex}/a_{hex} = 2.46$ for pseudo cubic $Sn_2Co_3S_2$ to 2.50 for Sn_2Co_3SSe. Cell volumes grow from 110 to 113 Å³ (iv).

Tab. 1. Predicted crystal structures for $Sn_2Co_3S_{2-x}Se_x$ (DFT)

Formula	$Sn_2Co_3S_2$	Sn_2Co_3SeS	$Sn_2Co_3Se_2$
Crystal sys.	trigonal	trigonal	trigonal
Space gr.	$R\bar{3}m$ (166)	$R3m$ (160)	$R\bar{3}m$ (166)
Spin	1/2	½	1/2
a_{rh}/Å	5.3762	5.4683	5.5635
α_{rh}/°	59.97	59.16	58.33
V_{rh}/Å³	109.80	113.42	117.11
a/Å	5.3738	5.3990	5.4322
c/Å	13.1719	13.4788	13.7975
z(S/Se)	0.2832	0.280/0.288	0.2874
ρ(calc.)	7.27 g/cm³	7.74 g/cm³	8.17 g/cm³

Tab. 2. Crystallographic data for $Sn_2Co_3S_{2-x}Se_x$ from X-ray powder diffraction

x	a_{hex}/Å	c_{hex}/Å	a_{rh}/Å	α_{rh}/°	V_{hex}/Å³	V_{rh}/Å³
0	5.366(1)	13.173(1)	5.374(1)	59.90(3)	328.5(1)	109.5
0.2	5.377(1)	13.248(1)	5.398(1)	59.74(2)	331.7(1)	110.6
0.4	5.383(1)	13.309(1)	5.417(1)	59.59(3)	333.9(1)	111.3
0.6	5.389(1)	13.374(1)	5.437(1)	59.43(2)	336.4(1)	112.1
0.8	5.397(1)	13.441(1)	5.457(1)	59.27(3)	339.0(1)	113.0
1	5.400(1)	13.494(1)	5.473(1)	59.13(3)	340.9(1)	113.6

Tab. 3. Calculated atomic site positions for Sn_2Co_3SeSe (DFT)

Atom	Wyckoff position	x	y	z
Sn	1a	-0.0007	x	x
Sn	1a	0.5088	x	x
Co	3b	-0.0037	x	-0.5011
Se	1a	0.2889	x	x
S	1a	-0.2803	x	x

Tab. 4. Atomic distances d/Å for $Sn_2Co_3S_{1-x}Se_x$ (DFT)

x =	0	1	2
Sn1-Co	2.689	3 x 2.722, 3 x 2.747	2.782
Sn1-S	3.171	3.192	
Sn1-Se		3.175	3.194
Co-Co	2.686	2 x 2.675, 2 x 2.724	2.711
Sn2-Co	2.686	2 x 2.704	2.711
Sn2-S	2.856	2.805	
Sn2-Se		2.979	2.934
Co-S	2.183	2.177	
Co-Se		2.292	2.286
S(e)-S(e)	3.371	3.374	3.378

For $In_xSn_{2-x}Co_3S_2$ an increase of c/a was also observed but a deviation from Vegard´s law was attributed to A site ordering for In and Sn.[4-9] This is not found for S/Se ordering. The experimental cell parameters fit well with the DFT predictions on $Sn_2Co_3S_2$ ($\bar{R}3m$), the mentioned model for Sn_2Co_3SSe ($R3m$) and hitherto unknown isotypic $Sn_2Co_3Se_2$ (Tab. 1). S/Se ordering does not break Vegard´s law interpolated to the complete substitution of S by Se. The good agreement of DFT predictions and experimental data encourages a closer look at the Sn_2Co_3SeS model (Tab. 2-4). The loss of the inversion centre reduces symmetry from $\bar{R}3m$ to $R3m$ and causes local structure distortions. Ch-M-Ch bonds are asymmetric now. Sn atoms on $1a$ (x1,x1,x1) and $1a$ (x2,x2,x2) are shift from the centres of inversion to x1 = -0.001 and $x2$ = 0.509 (Tab. 3). Co-S (2.18 Å) and Co-Se (2.30 Å) are similar to values of known $Sn_2Co_3S_2$ and predicted $Sn_2Co_3Se_2$, respectively (Tab. 4). The same relation is found for secondary bonds of Sn2 along c_{hex} to S (2.86 Å) and Se (2.91 Å) with respect to the parent compounds. Due to a shift of the Co atoms from the ideal (0,0,1/2) position the Kagomé lattice becomes distorted. Equal metal distances in $Sn_2Co_3S_2$ ($d_{Sn2-Co} = d_{Co-Co} = a_{hex}/2$ = 2.68 Å and $d_{Sn1-Co} = a_{rh}/2$ = 2.68 Å) split to 3+3 (2.72, 2.75 Å), the four Co-Co distances to 2+2 (2.67, 2.73 Å) in Sn_2Co_3SeS. Sn2-Co (2.70 Å) are slightly longer. Contrary to $Sn_2Co_3S_2$ angles deviate from linearity for Sn2-Co-Sn2 (177°), Sn1-Co-Sn1 (179°), and S-Co-Se (174°).

From present data one can conclude that a locally balanced substitution of S by Se is simple up to x(Se) =1. For x(Se) > 1 both interlayer sites are occupied by Se. This causes a weaker Co-Sn1 bonds and close Se-Se contacts. The final clarification of phase stability for x(Se) > 1 with respect to binary products and skutterudite type $Co_2Sn_3Se_3$[43] as shown for M = Ni, Pd, Pt compounds[24] remains subject of future work.

Magnetic properties

Questions on magnetic effects of S/Se substitution are answered from experimental DSC and susceptibility data. According to results form differential scanning calorimetry (DSC, Fig. 3a) for powder samples the Curie temperature T_c gradually decreases gradually in the solid solution $Sn_2Co_3S_{2-x}Se_x$ from 176(1) K (x = 0) to 142(2) K (x = 0.9). The values are obtained from heating and cooling curves differ with higher x(Se). This indicates an increasing hysteresis effect induced by Se (see also SI). Data from cooling curves coincides with T_C values obtained by magnetic susceptibility (χ) measurements (Fig. 3b, Table 5). Here, the ordering temperature was determined to decrease to 133(1) K for x= 0.9. The paramagnetic regimes of the susceptibility data were fitted with the Curie-Weiss law. In the case of $Sn_2Co_3S_{1.8}Se_{0.2}$ a modified Curie-Weiss law $\chi = \chi_0 + (C / (T-\theta))$ was applied where χ_0 accounts for a temperature independent contribution, most likely from a tiny impurity component (SnSe and Co_3Sn_2 according to X-ray diffraction, see SI). One has to keep in mind also known effects from the sample shape, as T_C = 172(1) K was found for a large single

crystal of $Sn_2Co_3S_2$ compared to TC = 177(1) K from powder samples.[14] Here even large errors of 20 K were reported.[15] This is explained by the large range of the magnetisation curves (Fig. 3b). the onset starts at 200 K, saturation is reached below 50 K. As seen previously[9,15] lower effective moments are obtained for powder samples compared to single crystal data.[14,17] This is attributed to the high magnetic anisotropy of the magnetism of Co shandites that reaches 0.92 μ_B along c_{hex} but vanishes within the a-b plane.[14] Due to statistical distribution of the particles, this effect is partially averaged in powders. Saturation is lowered and becomes field dependent. Besides T_C a clear effect of Se is seen from the magnetization isotherms that are depicted in Fig. 4. At 5 K we observe a pronounced hysteresis in all three cases with coercive field strengths of H_C = 16, 10 and 8 kOe from low to high Se content. In addition there are weak transitions upon reversing the direction of the magnetic field which might be due to anisotropy or the particle orientation, changing the domain structure. In contrast to the rectangular shape of the magnetization isotherms of the single crystal measurements,[14] the powdered samples exhibit curved ones. This is due to the statistic orientation within the polycrystalline samples with respect to the easy axis (H parallel c). We estimate a similar effect on the saturation magnetization (μ_{SM}) at 5 K (cf. Tab. 5).
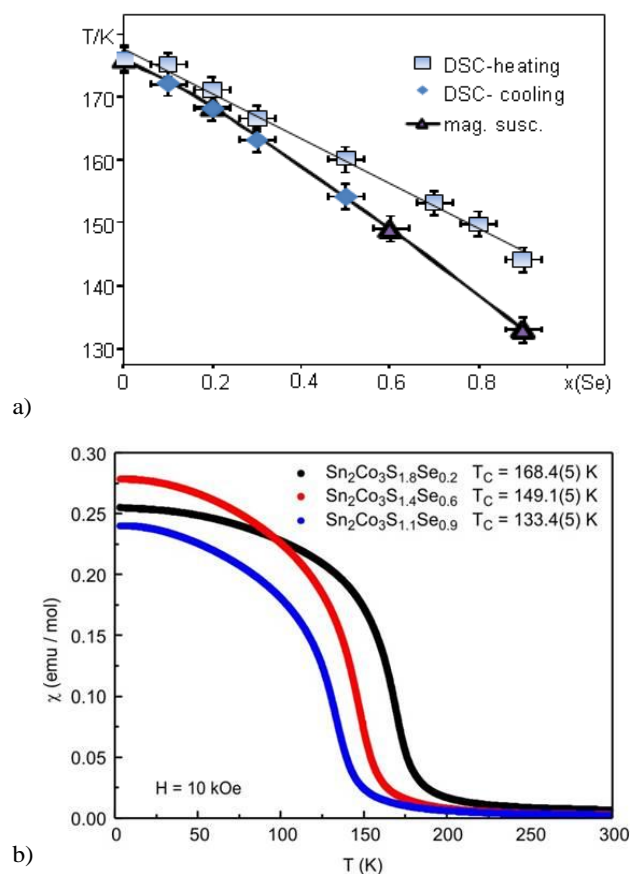

a)

b)

Fig. 3. a) Change in T_C for $Sn_2Co_3S_{2-x}Se_x$ from thermal analysis (DSC, powder samples) and temperature dependent magnetic

susceptibility (χ) data (b) at a magnetic flux density of 10 kOe. Lines mark the positions for T = 273 K and T = 77 K.

The decrease of the hysteresis with higher content of Se gives a significant hint that the spins are inverted more easily as a direct effect of weaker coupling between the Co layers. The 150 K magnetization isotherms show less pronounced curvature as they show the sample's behaviour close to or above their respective ordering temperatures. The 200 K isotherms display linear dependence of the magnetization with the applied field as is expected for paramagnetic materials.
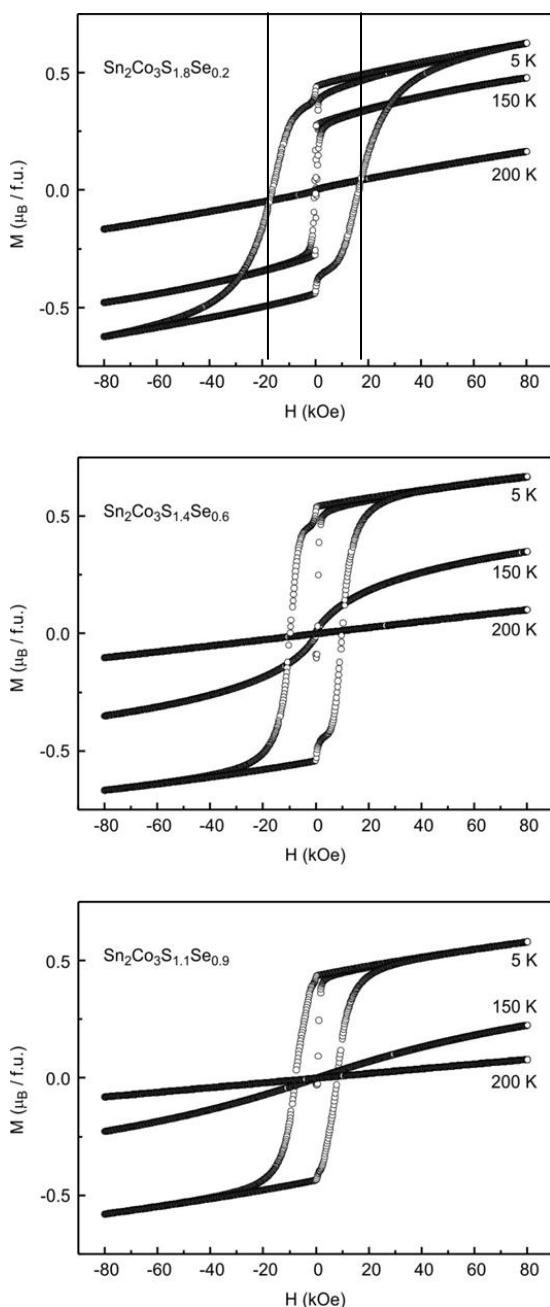

Fig. 4. Magnetization isotherms of the solid solution $Sn_2Co_3S_{2-x}Se_x$ measured at 5, 150 and 200 K with magnetic flux densities of up to 80 kOe.

Tab. 5. Measured magnetic properties for selected compositions $Sn_2Co_3S_{2-x}Se_x$ (x = 0.2, 0.6, 0.9) compared to powder (P) and single crystal (SC) data for $Sn_2Co_3S_2$.

	μ_{eff} (μ_B/)	θ_P (K)	T_C (K)	χ_0 (emu/mol)	μ_{SM} (μ_B/f.u.)
0 - SC[15]	1.72(1)		172	–	0.92
0 - P[15]		183(1)	177		
0 - P[9]	1.15(1)	180(20)	171		0.87
0.2 - P	1.08(1)	167.5(5)	168.4(5)	$3.48 \cdot 10^{-3}$	0.63(1)
0.6 - P	1.05(1)	147.8(5)	149.1(5)	–	0.67(1)
0.9 - P	1.05(1)	133.6(5)	133.4(5)	–	0.58(1)

^{119}Sn Mössbauer spectroscopy

Tab. 6. Fitting parameters of ^{119}Sn Mössbauer spectroscopic measurements of samples from the solid solution $Sn_2Co_3S_{2-x}Se_x$ at 298 and 78 K, δ = isomer shift, ΔE_Q = electric quadrupole splitting, Γ = experimental line width; B_{Hf} = magnetic hyperfine field. Values for CoSn impurity are taken from.[31] Parameters marked with asterisks were kept fixed during fitting procedure.

Compound	T (K)	δ (mm s^{-1})	ΔE_Q (mm s^{-1})	Γ (mm s^{-1})	B_{Hf} (T)	Area (%)
$Sn_2Co_3S_{1.8}Se_{0.2}$						
Sn-a	298	2.20(1)	2.06(1)	1.08(1)	–	46*
Sn-b	298	2.12(1)	2.55(1)	0.94(1)	–	46*
CoSn impurity	298	1.84*	1.56*	0.97(4)	–	8*
Sn-a	78	2.21(1)	2.26(1)	1.84(1)	10.8(1)	47(1)
Sn-b	78	2.22(1)	-2.56(1)	1.74(1)	33.3(1)	47(1)
CoSn impurity	78	1.88*	1.57*	1.23(4)	–	6(1)
$Sn_2Co_3S_{1.4}Se_{0.6}$						
Sn-a	298	2.17(1)	2.04(2)	1.15(2)	–	49.5*
Sn-b	298	2.15(1)	2.47(2)	0.95(1)	–	49.5*
CoSn impurity	298	1.84*	1.56*	0.81*	–	1*
Sn-a	78	2.17(1)	2.53(2)	2.80(2)	8.9(1)	51(1)
Sn-b	78	2.24(1)	–2.55(2)	2.66(3)	30.0(1)	48(1)
CoSn impurity	78	1.88*	1.57*	0.80*	–	1(1)
$Sn_2Co_3S_{1.1}Se_{0.9}$						
Sn-a	298	2.20(1)	2.03(2)	1.36(3)	–	48*
Sn-b	298	2.15(1)	2.39(1)	0.89(2)	–	48*
CoSn impurity	298	1.84*	1.56*	0.81*	–	4*
Sn-a	78	2.16(1)	2.43(2)	2.83(3)	7.7(1)	50(1)
Sn-b	78	2.16(1)	–2.59(2)	2.82(4)	26.8(1)	46(1)
CoSn impurity	78	1.88*	1.57*	0.92(5)	–	4(1)

The experimental and simulated ^{119}Sn-Mößbauer spectra of $Sn_2Co_3S_{2-x}Se_x$ with x = 0.2, 0.6, and 0.9 at room temperature and T = 78 K are presented in Fig. 5. The corresponding fitting parameters are listed in Table 3. Similar to the parent compound $Sn_2Co_3S_2$,[14] and paramagnetic $Sn_2Ni_3S_2$[15] the spectra of the solid solution could be well reproduced by a

superposition of two signals with different quadrupole splitting parameters. All three samples showed small degrees of a Co-Sn impurity phase. Since the spectral contribution of the impurity phase was small, independent refinement of the isomer shift and quadrupole splitting parameters was not possible. These data were constrained at the literature values for pure CoSn.[31-32] Sulphur substitution by selenium has only little influence on the isomer shift and the quadrupole splitting parameter.

From the obtained values for the solid solution $Sn_2Co_3S_{2-x}Se_x$ the crystallographically independent positions cannot be distinguished in the paramagnetic regime. Isomer shifts ($\delta_{1,2}$ = 2.2 mms^{-1}) and the large quadrupole splitting (ΔE_Q > 2.0 mms^{-1}) are similar. However, they differ significantly in the ferromagnetic regime at T = 77 K in the transferred hyperfine fields and in the quadrupole moments (sign and value). The hyperfine fields decrease from 34.2 to 26.8 T for one and from 11.2 to 7.7 T for the other Sn site in the sequence x = 0.2 → 0.6 → 0.9. This decrease is related to a geometrical effect, in contrast to the In / Sn substitution which leads to a decrease in the valence electron count.[20] It mirrors the macroscopic magnetisation at the local scale that is far from saturation for x = 0.9 at T = 77 K.. As subsequently shown macroscopic and microscopic magnetisation are directly related.

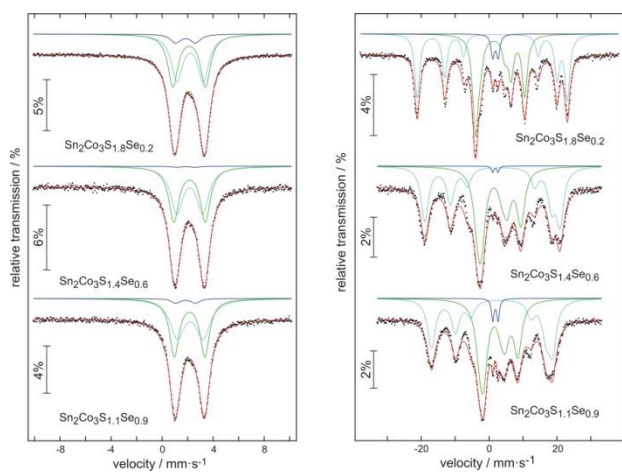**Fig. 5.** Experimental and simulated ^{119}Sn Mössbauer spectra for samples from the solid solution $Sn_2Co_3S_{2-x}Se_x$ at room temperature (left) and T = 77 K (right). Green and light-blue lines correspond to the tin sites Sn2 and Sn1. The CoSn impurity signal is drawn by a dark-blue line.

DFT calculations

A straightforward interpretation of the experimentally observed magnetisation behaviour and Mößbauer spectra is delivered from spin polarised DFT calculations on $Sn_2Co_3S_2$, Sn_2Co_3SSe, and $Sn_2Co_3Se_2$. They are predicted as novel HFM with S = 1/2 ground states similar to $Sn_2Co_3S_2$.[2,14] In Fig. 6 a, the calculated electronic energy is plotted upon stepwise increase of spin

moments M = 2*S = n_α-n_β. The minimum in energy is found at M = 1 in each case. The gain in energy with respect to the non spin polarised state (M = 0) is lowered for $Sn_2Co_3Se_2$ (41 meV) compared to Sn_2Co_3SeS (49 meV) and $Sn_2Co_3S_2$ (53 meV). These results correspond to the experimentally observed decrease of T_C with increasing x(Se). Calculations with spin orbit coupling (SOC) confirm the gain in energy. Additionally, they indicate a higher orbital moment for Sn_2Co_3SSe (-0.12 μ_B) compared to $Sn_2Co_3S_2$ (-0.06 μ_B, see ESI S7).
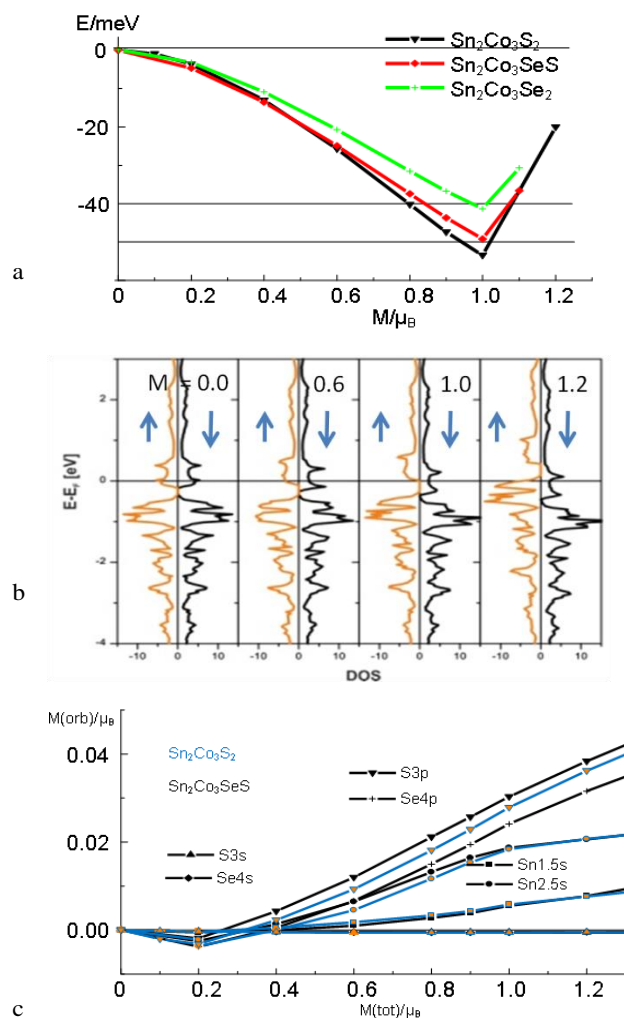
Fig. 6. a) Calculated gain in energy E(M) from fixed spin calculations on $Sn_2Co_3S_2$, Sn_2Co_3SeS, and $Sn_2Co_3Se_2$ (0 ≥ M = $n_\alpha - n_\beta$ ≤ 1.4), b) spin resolved DOS (up and down spin) for Sn_2Co_3SeS at m = 0, 0.5, 1.0, 1.4; c) Spin polarisation of the Sn1-, Sn2-5s, S-3sp- and Se-4sp orbitals as a function of the total spin polarisation in $Sn_2Co_3S_2$ (blue lines) and Sn_2Co_3SeS.

DOS plots for the fixed spin states M = 0, 0.6, 1.0, 1.2 (Fig. 6b) visualize the change from spin degenerated (M = 0) to the HFM (M = 1) state for Sn_2Co_3SeS. The additional electrons compared to semiconducting $InSnCo_3S_2$ as mentioned in Fig. 1 are found in the bands above the pseudo gap. By the loss of spin degeneracy these electrons become spinpolarised. They create magnetic moments as mentioned in Fig. 1 as a consequence of

differences in occupation of α- and ß-Spin (M = $n_α$-$n_ß$). In the HFM states semiconducting spin channels are found with gaps of 0.37 eV ($Sn_2Co_3S_2$), 0.30 eV (Sn_2Co_3SeS), and 0.24 eV ($Sn_2Co_3Se_2$). Consequently, Se orbitals have an effect on the bands at E_F and to spin polarisation. What are these states?

Fig. 6c shows the spin polarisation M(orb) of selected orbitals as a function of the total macroscopic magnetisation M(tot). Accordingly, Sn-5s, S-3d, and Se-4d orbitals are spin polarised with increasing M(tot). They have the same spin direction like Co-$3d_{z^2}$ and $3d_{x^2-y^2}$ orbitals that cover > 90 % of the total spin polarisation in Sn_2Co_3SeS (see SI). One must conclude on direct exchange by bonding in the [$CoSSeSn_4$] polyhedra (Fig. 1d-f). The different contributions are in line with the Rhodes-Wohlfahrt-plot that indicates partly localised and delocalised magnetism for $Sn_2Co_3S_2$.[10] Fig. 6c further indicates lower spin polarisation for Se-4p than for S-3p. This signals an influence on the observed weakening of the magnetisation with higher x(Se) content.

The spin polarisation of the Sn1-5s and Sn2-5s orbitals serves as the key to the hyperfine splitting from [119]Sn Mößbauer spectroscopy. Due to their non-vanishing wave function the Sn-5s orbitals transfer magnetic moments to the cores by Fermi contact of the spin density [$ρ(r)_α$-$ρ(r)_ß$] (Eq. 1).[33] Calculated values for the spin polarisation of Sn1-5s and Sn2-5s (Fig. 6c) increase for both Sn sites with the total magnetisation of Sn_2Co_3SSe. The lower hyperfine fields found for $SnCo_3S_{1.1}Se_{0.9}$ at 77 K are thus attributed to lower macroscopic magnetisation. At full magnetisation (M = 1) the calculated orbital spin polarisation behaves like 1:3 for Sn1-5s and Sn2-5s. This reflects the ratio obtained for the hyperfine fields of the two Sn sites in $Sn_2Co_3S_2$ (12 T : 36 T). The larger field (Sn-b) is thus attributed to Sn2 within the layers and the lower (Sn-a) to Sn1 between the layers. The assignment rationalizes the considerations given in Fig. 1b-c that two Co triangles are linked by Sn1, but six Co triangles by Sn2.

$$ΔE_{hf} = 8/3 \; πμ_e \; m(r = 0) = \{16/3 πμ_B(ρ_α(0) - ρ_ß(0))\} 2 πgμ_N I/h \quad (Eq. 1)$$

$$δ = k * Δρ(r) = k * [ρ^q(r)_s - ρ^q(r)_r] \quad\quad (Eq. 2)$$

$$ΔE_Q = ½ \; eQV_{zz}(1+ 1/3 \; η^2)^{½} \quad (with \; η= (V_{xx}-V_{yy})/V_{zz} = 0) \quad (Eq. 3a)$$

$$½(n(p_x)+n(p_y))-n(p_z) \sim V_{ZZ} \quad\quad (Eq.3b)$$

Fermi contact also plays the key role to interpret the Mößbauer isomer shift δ. Eq. 2[34-36] relates δ and Fermi contact density [$ρ(r)_s$-$ρ(r)_r$] with respect to $CaSnO_3$ as Sn(+IV) reference. Values of δ deviate for different valence states of Sn mainly due to changes in the occupation of the 5s orbitals. In line with the non differing $δ_{1,2}$ values similar 5s orbital occupation numbers of 1.6 e are calculated for Sn1 and Sn2 atoms in $Sn_2Co_3S_2$ and Sn_2Co_3SeS. To clarify questions on valences and charges therein calculated values and experimentally known isomer shifts are compared in Fig. 7a for typical compounds for Sn(+IV) like SnO_2 (δ = 0 mms^{-1}) and SnS_2 (1.3 mms^{-1}), Sn(0) in α-Sn (2.0 mms^{-1}) and ß-Sn (2.55 mms^{-1}), and Sn(+II) in SnS

(3.3 mms^{-1}) and $SnCl_2$ (4.05). Isotypic $Sn_2Ni_3S_2$ ($δ_{1,2}$ = 2.48 mms^{-1})[15] is included due to its higher isomer shift. Indeed a higher Sn-5s orbital occupation (1.7) is calculated than for the $Sn_2Co_3Ch_2$ compounds. From experimental δ and calculated 5s values Sn atoms in the shandites are found between α-Sn and ß-Sn and to a broader range between SnS and SnS_2. From the present method that probes the charge density at the core, the states are closer to Sn(0) than to Sn(+II). How is this understood with respect to formal valence considerations[41] where one might conclude on Sn(+II) in the shandites?[44]

a

b

c
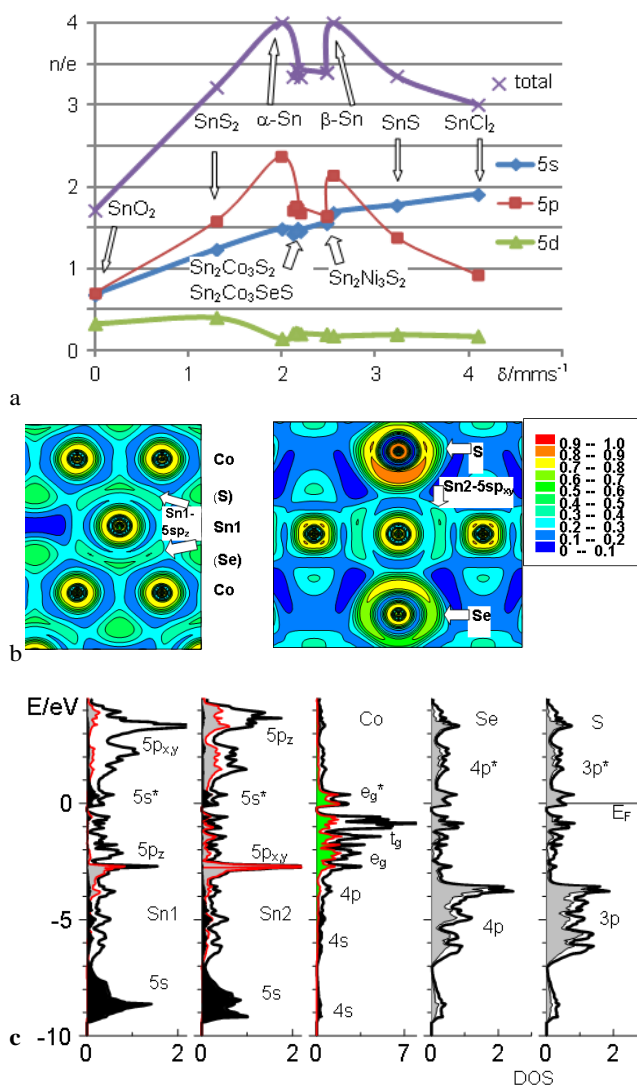
Fig. 7. a) Calculated integrated orbital occupation for Sn-5s, 5p-, and 5d orbitals and summed Sn-5spd occupation in various Sn compounds; b) ELF plots for Sn1 (l., with Co atoms of neighboured Co layers), and Sn2 (r., with Co, S, and Se neighbours); c) atomic site and orbital projected density of states for Sn_2Co_3SeS;

With the different meaning of valence and charge in mind, we look at atomic charges. Calculated values are +0.65, +0.6, and +0.7 for the Sn atoms in $Sn_2Ni_3S_2$, Sn_2Co_3SeS and $Sn_2Co_3S_2$,

respectively, from orbital analysis (and Bader-AIM integration). Reasons are found in Fig. 7a from the Sn-5p occupation. These numbers decrease form Sn(0) to Sn(IV) and Sn(+II) due to increasing ionicity. Again, the occupation of Sn-5p orbitals in the shandites (1.7 e) is higher than in SnS or SnS_2 but lower than in α-Sn or ß-Sn.

Found charges and Sn-5p orbital occupation numbers are understood from local anisotropy and the electric field gradients of the Sn1 and Sn2 sites in Sn_2Co_3SeS. According to Eq. 3a-b measured quadrupole splitting values are proportional to calculated V_{ZZ} components of the EFG[35-38] and to the difference in orbital occupation $1/2 (n(px)+n(py)) - n(p_z)$. The sign of the quadrupole splitting is determined in the ferromagnetic shandites due to an internal magnetic field. With[39] $Q = -10.9(8)$ fm² the measured positive value of $\Delta E_Q = 2.43$ has to be attributed to the calculated value $V_{ZZ}(Sn1) = -2.3*10^{22}$ V/m² and $\Delta E_Q = -2.55$ to $V_{ZZ}(Sn2) = +3.1*10^{22}$ V/m². The assignment from the hyperfine values is confirmed. In agreement with experimental data calculated V_{ZZ} values and orbital occupation numbers are similar for $Sn_2Co_3S_2$ and Sn_2Co_3SeS (ESI, S8).

The differences in bonding for Sn1 and Sn2 are visualised from the analyses of the electron localisation function (ELF, Fig. 7b). Accordingly, the Sn-5s orbitals do not behave like spherical lone pairs as expected for ionic Sn(+II). They form hybride $Sn1-5sp_z$ and $Sn2-5sp_{x,y}$ orbitals and multi-centre-bonds to neighbouring Co atoms. No ELF maxima are detected for $Sn1-5p_{x,y}$ and $Sn2-5p_z$ orbitals that point to S and Se neighbours.

The received results can be summarized from the atomic and orbital projected density of states (Fig. 7c). The loss of degeneracy of the Sn-5p orbitals is shown by a shift of the less occupied $Sn1-p_{x,y}$ and $Sn2-p_z$ states above E_F (for integrated values see ESI-S8 and results for $InSnCo_3S_2$[7,20]). Respective DOS maxima at 2.7 eV are due to $Sn1-p_z$ orbitals that form bonds to Co-3d states in the triangles above and below, and $Sn-5p_{x,y}$ orbitals that form bonds to the Co neighbours in the plains (compare Figs. 1b-c).[7, 8, 20] Consequently, the inverted coordination of Sn1 and Sn2 (Fig. 1b, c) causes signs and values of ΔE_Q and V_{ZZ} as given in Eq. 3b.[35,38,39] It causes also the observed charges. One must conclude that the Sn atoms in the shandites behave ionic like Sn(+II) towards S and Se neighbours, but covalent like Sn(0) to Co neighbours. The decisive valence state above the gap are formed by Co-3d e_g like states (d_{z^2}, $d_{x^2-y^2}$) that interact with Sn-5s, Se-4p, and S-3p orbitals in the tetragonal bipyramide coordination $CoSeSSn_4$. The reason for the isomer shift and the hyperfine fields of the Sn atoms is found in their antibonding contributions to states above E_F. This causes a lower occupation than 5s² for ionic Sn(+II) and it allows for high spin polarisation. The larger hyperfine fields of Sn2 correlate with the higher contributions the DOS maximum at E_F compared to Sn1-5s. The Co atoms are confirmed in a Co(0) state (calculated charge -0.2). S (-0.4) is more ionic than Se (-0.1), but both are not in typical ionic states. Se-4p and S-4p orbitals are not fully occupied but contribute to antibonding states above E_F. Most likely, the Co shandites are best described as anisodesmic[45] bond systems with covalent Co-S(e), metallic Co-Sn, and ionic Sn-S(e) interactions. In accordance with the atomic bonding situation the *Ch* atoms also behave like a chameleon: as *Ch*(0) towards Co and as *Ch*(-II) to S neighbours.

Conclusions

Crystal structure effects and magnetic properties are shown to be coupled for the solid solution of $Sn_2Co_3S_{2-x}Se_x$ (x = 0;1) from experimental data and DFT calculations. From X-ray an increaling c/a ratio is found. Contrary to In/Sn ordering in $InSnCo_3S_2$ assumed S-Se ordering in Sn_2Co_3SeS does not cause a deviation of cell parameters from Vegard´s law. The maximum content x(Se) = 1 is rationalized from crystal structure considerations. According to magnetic measurements Curie temperatures and magnetic hysteresis decrease with increasing x(Se) content. [119]Sn-Mößbauer spectra indicate high anisotropy and magnetic fields for Sn atoms in and between the Co layers. The S/Se substitution is shown to cause weaker interlayer coupling. Despite of local and crystal structure distortions Sn_2Co_3SeS and $Sn_2Co_3Se_2$ are predicted as half metal ferromagnets from DFT calculations. The gain in energy upon spin polarisation is lowered with x(Se). For Se weaker ionicity and magnetisation of the 4p orbitals is found in comparison to S. Results from [119]Sn Mössbauer spectroscopy are interpreted from orbital and electronic structure analyses. Isomer shifts and hyperfine coupling are explained from bonding contributions of Sn-5s orbitals that are not fully occupied lone pairs as expected for ionic Sn(+II). Together with Sn-5p orbitals they form multi-center bonds to Co neighbours. At the same time Sn-5p orbitals that point to S and Se neighbours are shift to unoccupied states. This causes high bonding anisotropy and quadrupole moments. $Sn_2Co_3S_{2-x}S_x$ is shown as a system to tune unconventional magnetism with anistropic coupling. The anisodesmic characteristics with metal-chalcogene (Co-S, Sn-S) and metal-metal (Co-Sn, Co-Co) bonds is described by coordination spheres $SnCo_6S_8$, $CoSn_4S_2$ and $[SCo_3Sn_8]$ in the perovskite related HAP model.

Acknowledgements

Notes

a) Universität Regensburg, Institute of Inorganic Chemistry,

Universitätsstraße 31, 93040 Regensburg, Germany,

Fax: +49-941-943-4983.

*Email:richard.weihrich@ur.de

Homepage:www.uni-regensburg.de/Anorganische_Chemie/Weihrich/.

b) Department für Chemie, TU München, Lichtenbergstr. 4, 85748 Garching b. München, Germany.

c) Institut für Anorganische und Analytische Chemie, Universität Münster, Corrensstrasse 30, D-48149 Münster, Germany E-mail: pottgen@uni-muenster.de

References

1. (a) J. Liu, T. Gottschall, K. P. Skokov, J. D. Moore and O. Gutfleisch, *Nat. Mater.* 2012, **11**, 620-626; (b) T. Nilges, S. Lange, M. Bawohl, J.-M. Deckwart, H.-D. Wiemhöfer, R. Decourt, B. Chevalier, J. Vannahme, H. Eckert, and R. Weihrich: $Ag_{10}Te_4$ Br_3: *Nat. Mater.* 2009, **8**, 101-8.

2. a) R. Weihrich, S. F. Matar, V. Eyert, F. Rau, M. Zabel and M. Andratschke, I. Anusca and T. Bernert, *Prog Solid State Chem*, 2007, **35**, 309-327. b) R. Weihrich, I. Anusca and M. Zabel, *Z. Anorg. Allg. Chem.*, 2005, **631**, 1463-1470. c) S. Seidlmayer, F. Bachhuber, I. Anusca, J. Rothballer, M. Bräu, P. Peter, R. Weihrich. Z Krist. 2010, **225**, 371-381.

3. a) T. Sakamoto, M. Wakeshima and Y. Hinatsu, *J. Phys. Condens. Matter* 2006, **18**, 4417. T. Sakamoto, M. Wakeshima, Y. Hinatsu and K. Matsuhira, *Phys. Rev. B.* 2008, **78**, 024509. a) S. Natarajan, G. V. S. Rao, R. Baskaran and T. S. Radhakrishnan, *J. Less-Common Met.*, 1988, **138**, 215-224.

4. R. Weihrich and I. Anusca, *Z Anorg Allg Chem*, 2006, **632**, 1531-1537.

5. M. Fujioka, T. Sibuya, J. Nakai, K. Yoshiyasu, Y. Sakai, Y. Takano, Y. Kamihara and M. Matoba, *Solid State Commun.* 2014, **199**, 56–60.

6. a) J. Corps, P. Vaqueiro and A. V. Powell, *J. Mater. Chem. A*, 2013, **1**, 6553-6557. b) J. Corps, P. Vaqueiro, A. Aziz, R. Grau-Crespo, W. Kockelmann, J.-C. Jumas, and A. V. Powell, Chem. Mater. 2015, DOI: 10.1021/acs.chemmater.5b00801.

7. J. Rothballer, F. Bachhuber, F. Pielnhofer, F. M. Schappacher, R. Pöttgen and R. Weihrich, *Eur. J. Inorg. Chem.*, 2013, **2**, 248-255.

8. J. Rothballer, F. Bachhuber, S. M. Rommel, T. Söhnel and R. Weihrich. *RSC Adv.* 2014, **4**, 42183-42189.

9. T. Kubodera, H. Okabe, Y. Kamihara and M. Matoba, *Physica B* 2006, **378–380**, 1142–1143.

10. M. Matoba, A. Umetani, E. Nagoshi and T. Kubodera, *Phsica B*, 2008, **403**, 1356-1358.

11. F. Pielnhofer, A. S. Tragl, J. Rothballer and R. Weihrich, *Z. Naturforsch. B*, 2014, **69**, 55-61.

12. P. Gütlich, K.-J. Range, C. Felser, C. Schultz-Munzenberg, W. Tremel, D. Walcher and M. Waldeck, *Angew. Chem.* 1999, **111**, 2524; *Angew. Chem. Int. Ed.* 1999, **38**, 2381.

13. Y. Saka, R. Tanakadate, M. Matoba, I. Yamada, N. Nishiyama, T. Irifune, K. Funokoshi, T. Kunimoto, Y. Higo and Y. Kamihara, *J. Phys. Soc. Jpn.* 2015, **84**, 044705.

14. W. Schnelle, A. Leithe-Jasper, H. Rosner, F. M. Schappacher, R. Pöttgen, F. Pielnhofer and R. Weihrich, *Phys. Rev. B.* 2013, **88**, 205116.

15. P. Vaqueiro and G. G. Sobany, *Solid State Sci.*, 2009, **11**, 513-518.

16. M. Holder, Yu. S.Dedkov, A.Kade, H.Rosner, W. Schnelle, A. Leithe-Jasper and R. Weihrich, S. L. Molodtsov, *Phys. Rev. B* 2009, **79**, 205116-9.

17. X. Lin, S. L. Budko, and P. C.Canfield, *Phil. Mag.*, 2012, **92**, 2436.

18. A. K. Arzhnikov, L. V. Dobysheva F. Brouers, *Phys. Solid State*, 2000, **42**, 89-95.

19. (a) S. Mukhopadhyay, G. P. Das, S. K. Ghosh, A. Paul and A. Gupta, *J. Magn. Magn. Mater,* 2002, **246**, 317–326; (b) S. Mukhopadhyay S., D. Nguyen-Manh, *Phys. Rev. B*, 2002, **66**, 1444081-10.

20. F. Pielnhofer, J. Rothballer, P. Peter, W. Yan, F. M. Schappacher, R. Pöttgen and R. Weihrich, *Z. Anorg. Allg. Chem.*, 2014, **640**, 286-294.

21. Y. Sakai, Y. Kamihara and M. Matoba, *Physica status solidi c*, 2013, **10**, 1130-1131.

22. T. Sato, J. Lynn, Y. Hor and S.-W. Cheong, *Phys Rev B*, 2003, **68**, 214411.

23. S. Ronneteg, M.-W. Lumey, R. Dronskowski and R. Berger, *J. Magn. Magn. Mater.*, 2006, **303**, 204-213.

24. R. Weihrich, I. Anusca and M. Zabel, *Z. Anorg. Allg. Chem.*, 2005, **631**, 1463-1470.

25. V. Petříček, M. Dušek and L. Palatinus, *Z. Kristallogr.*, 2014, **229**, 345-352. b) Petricek, V., Dusek, M. & Palatinus, L. (2014). Z. Kristallogr., *2014*, **229**, 345-352.

26. J. P. Perdew, K. Burke and M. Ernzerhof, *Phys Rev Lett*, 1996, **77**, 3865-3868.

27. V. R. S. R. Dovesi, C. Roetti, R. Orlando, C. M. Zicovich-Wilson, F. Pascale, B. Civalleri, K. Doll, N. M. Harrison, I. J. Bush, P. D'Arco, M. Llunell, M. Causà and Y. Noël, *University of Torino*, 2014, **Torino**

28. H. E. K. Koepernik, *Phys. Rev. B*, 1999, **59**, 1743–1757.

29. K. K. I. Opahle and H. Eschrig, *Phys. Rev. B*, 1999, **60**, 14035–14041.

30. O. Osters, T. Nilges, M. Schöneich, P. Schmidt, J. Rothballer, F Pielnhofer and R. Weihrich, *Inorg. Chem.*, 2012, **51**, 8119-8127.

31. L. Häggström, T. Ericsson and R. Wäppling, *Phys Scripta*, 1975, **11**, 94.

32. Djegamar.C, P. Lecocq and A. Michel, *Ann Chim France*, 1969, **4**, 175.

33. a) J. Terra and D. Guenzburger, *J. Phys.: Condens. Matter*, 1991, **3**, 6763–6774.

34. J. A. Gómez and D. Guenzburger; *Phys. Rev. B*, 2001, **63**, 1344041-10.

35. R. Weihrich, S. Lange and T. Nilges, *Solid State Sci.*, 2009, **11**, 519-27.

36. P.E. Lippens, *Phys. Rev. B,* 1999, **60**, 4576–4586.

37. A. Svane, N.E. Christensen, C.O. Rodriguez and M. Methfessel, *Phys. Rev. B*, 1997, **55**, 12572–12577.

38. P. Blaha, K. Schwarz, W. Faber and J. Luitz, *Hyperfine Interact.*, 2000, **126**, 389–395.

39. H. Haas, M. Menningen, H. Andreasen, S. Damgaard, H. Grann, F. T. Pedersen, J. W. Petersen and G. Weyer, *Hyperfine Interact.*, 1983, **15**, 215-18.

40. E. A. Owen, D. Madoc Jones, *Proc. Phys. Soc.*, 1954, **67**, 456-466.

41. M. Armbruester, W. Schnelle, R. Cardoso-Gil, Yu. Grin, *Chem. Eur. J.*, 2010, **16**, 10357-10365.

42. H. Fjellvag, A. Kjekshus, *Acta Chem. Scand. A*, 1986, **40**, 23-30.

43. F. Laufek, J. Navratil, J. Plasil, T. Plechacek, C. Drasar, J. Alloys Comp., 2009, **479**, 102-106

44. M. Jansen, U. Wedig, *Angew. Chem.* 2008, **120**, 10176-80, *Angew. Chem. Int. Ed.* 2008, **52**, 10026-29.

45. A. Baranov, M. Kohout, F. R. Wagner, Y. Grin, R. Kniep, W. Bronger, Z. Anorg. Allg. Chem. 2008, 634, 2747-53.